JOURNAL OF MATERIALS SCIENCE **40** (2005) 1169–1175

Corrosion behavior of carbon implanted ZIRLO alloy in 1 M H_2SO_4

D. Q. PENG*, X. D. BAI
Department of Materials Science and Engineering, Tsinghua University, Beijing, 100084, People's Republic of China
E-mail: pdq01@mails.tsinghua.edu.cn; baixde@mail.tsinighua.edu.cn

B. S. CHEN
Jianzhong Chemical Cooperation, Yibin, 644000, People's Republic of China

In order to study the effect of carbon ion implantation on the aqueous corrosion behavior of ZIRLO alloy, specimens were implanted with carbon ions with fluence ranging from 1×10^{16} to 1×10^{17} ions/cm^2, using a metal vapor vacuum arc source (MEVVA) at an extraction voltage of 40 kV. The valence states and depth distributions of elements in the surface layer of the samples were analyzed by X-ray photoelectron spectroscopy (XPS) and auger electron spectroscopy (AES), respectively. Transmission electron microscopy (TEM) was used to examine the microstructure of the carbon-implanted samples. Glancing angle X-ray diffraction (GAXRD) was employed to examine the phase transformation due to the carbon ion implantation. The potentiodynamic polarization technique was employed to evaluate the aqueous corrosion resistance of implanted ZIRLO alloy in a 1 M H_2SO_4 solution. It was found that a significant improvement was achieved in the aqueous corrosion resistance of ZIRLO alloy implanted with carbon ions. The higher the fluence, the worse is the corrosion resistance. Finally, the mechanism of the corrosion behavior of carbon-implanted ZIRLO alloy was discussed.

1. Introduction

ZIRLO alloy is widely used in the nuclear industry because of their low thermal neutron capture cross section, favorable mechanical properties, and good corrosion resistance. For example, ZIRLO alloy can serve as fuel cladding, spreaders for fuel elements, and for core-structure materials. However, with the concept of high burn-up fuel developing, improvements in the performance of ZIRLO alloy is increasingly required. It is well known that ion beam surface processing (IBP) techniques can significantly improve corrosion resistance [1–4]. Ion implantation offers the possibility to introduce a controlled concentration of an element to a thin surface layer. It was first shown, by Ashworth *et al.* [5], that chromium implantation could improve the corrosion resistance of iron. Additional studies of palladium implanted into titanium [6] and phosphorus implanted into iron [7] have confirmed that ion implantation with palladium or phosphorus may successfully improve the corrosion behavior.

It was reported that carbon implantation improved the corrosion resistance and tribological properties of steels, titanium, aluminum, etc. [8–10]. While relatively few papers have reported on the corrosion behavior of carbon-implanted ZIRLO alloy.

In this paper, we report the results of a study of carbon implantation on the aqueous corrosion behavior of ZIRLO alloy. The valence states of carbon, zirconium, and oxygen were analyzed by X-ray photoelectron spectroscopy (XPS), the depth distributions of elements in the surface layer were determined by Auger electron spectrometry (AES), and the corrosion resistance of the implanted ZIRLO alloy was investigated by the instrument of IM6e potentiostat. Transmission electron microscopy (TEM) was carried out to observe the micro-structure of the carbon-implanted samples. 0.3° Glancing angle X-ray diffraction (GAXRD) was employed to examine the phase transformation due to the carbon ion implantation. The mechanism of corrosion behavior of carbon-implanted ZIRLO alloy in the aqueous is discussed.

2. Experimental procedure

ZIRLO alloy samples were machined to a size of 10 mm × 10 mm from a 1 mm sheet of ZIRLO alloy, fully annealed after cold rolling. The composition of ZIRLO alloy is Nb 0.99 wt%, Sn 0.98 wt%, Fe 0.11 wt%, Cr 0.008 wt%, Si 0.003% wt%, O 0.11 wt%, C 0.007 wt%, balanced with zirconium. The ZIRLO alloy samples

*Author to whom all correspondence should be addressed.

TABLE I Implantation conditions

Fluence (ions/m^2)	1×10^{20}	5×10^{20}	1×10^{21}
Beam current density (μA/cm^2)	9	18	27
Temperature (°C)	100	220	250

were mechanically polished using 200–800 grid emery paper. The samples were then degreased in acetone and ethanol, chemically polished in a solution of 5% H_2SO_4, 10% HF, 30% HNO_3 and 55% H_2O by volume, and finally rinsed in deionized water.

For implantation the samples were loaded onto an aluminum sample holder with a diameter of 12 cm. The vacuum level of the MEVVA (Metal Vapor Vacuum Arc) implanter target chamber was 1.3×10^{-3} Pa. Although the implantation system has no magnet analytic capability, the extracted carbon ions are expected to consist of 100% C^+. Fluences of 1×10^{16}, 5×10^{16}, and 1×10^{17}ions/cm^2 were used. The extraction voltage for the carbon implantation was 40 kV. Therefore, the implantation energies were 40 KeV. The samples were not cooled during implantation. The implantation temperature therefore depended on the beam current density, which varied from 9 to 27 μA/cm^2. Table I summarized the implantation conditions used.

The valence states of carbon, zirconium, and oxygen on sample surfaces were analyzed by X-ray photoelectron Spectroscopy (XPS). The micro-structure of implanted samples was investigated using transmission electron microscope (TEM). The potentiodynamic polarization measurements were carried out to investigate the aqueous corrosion resistance of the carbon-implanted ZIRLO alloy. The potentiodynamic tests were performed in a 1 M H_2SO_4 solution using IM6e potentiostat (Zahner Electrik) at room temperature (25°). The solution was stirred up with pure nitrogen for an hour before the measurement. The tested area was 1 cm^2 and the scan rate was 2 mV/s. All electrochemical potential measurements were taken with respect to a saturated calomel electrode (SCE). Measurements were carried out using anode scan started in a cathodic region at approximately -0.4 V with respect to the SCE, and then scanned into the anodic region of approximately $+2.0$ V with respect to the SCE.

3. Results and discussion

3.1. The valence of the elements in the surface layer

To compensate for a systematic error in XPS measurement, the energy position was first adjusted by comparing the binding energy of the C 1s peak to that of the standard binding energy, 285 eV. The adjusted XPS spectra of C 1s, Zr $3d_{5/2}$, Nb $3d_{5/2}$ and O 1s are shown in Figs 1–4 respectively. The adjusted binding energy of Zr $3d_{5/2}$ is 182.3 eV (Fig. 2), coincides with the standard values of ZrO_2 [11], from which it is suggested that zirconium in the surface exists in the form of ZrO_2. The adjusted binding energy of Nb $3d_{5/2}$ is 206.9 eV (Fig. 3), coincides with the standard values of Nb_2O_5. from which it is suggested that niobium in the surface exists in the form of Nb_2O_5. Fig. 4 shows that

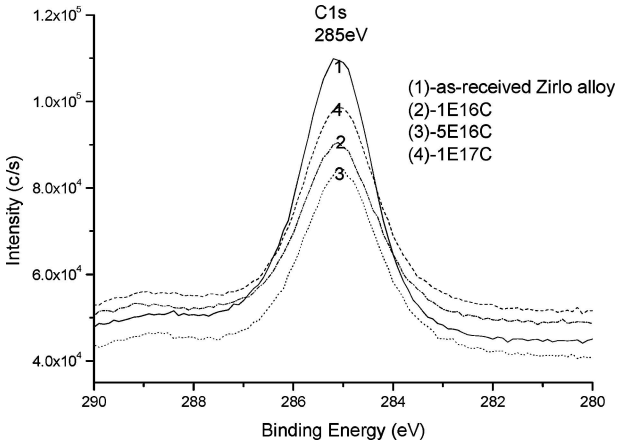

Figure 1 The XPS spectra of C 1s peak in the implanted surface: (1) as-received ZIRLO alloy; (2) carbon ions implanted with 1×10^{16} ions/cm^2;(3) carbon ions implanted with 5×10^{16} ions/cm^2; (4) carbon ions implanted with 1×10^{17} ions/cm^2.

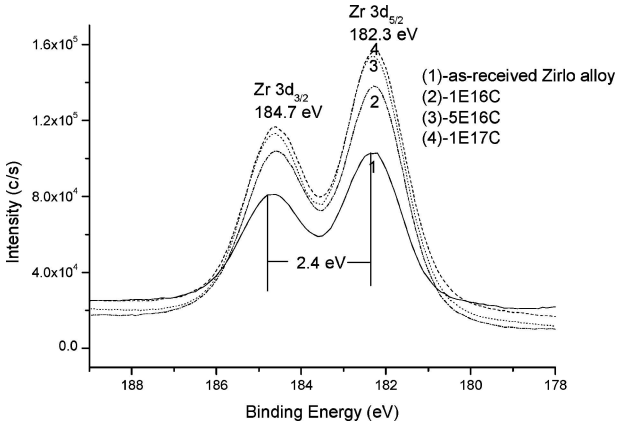

Figure 2 The XPS spectra of Zr $3d_{5/2}$ peak in the implanted surface: (1) as- received ZIRLO alloy, (2) carbon ions implanted with 1×10^{16} ions/cm^2; (3) carbon ions implanted with 5×10^{16} ions/cm^2;(4) carbon ions implanted with 1×10^{17} ions/cm^2.

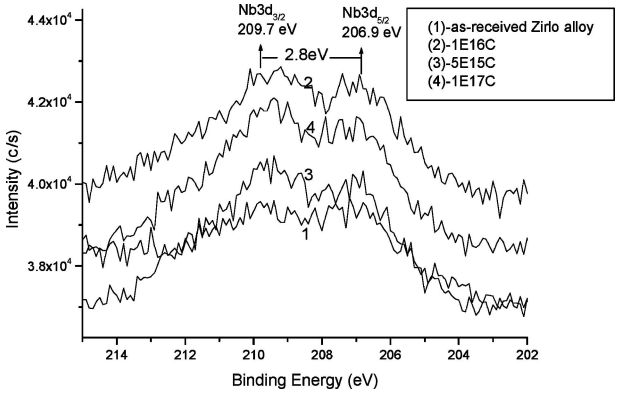

Figure 3 The XPS spectra of Nb $3d_{5/2}$ peak in the implanted surface: (1) as- received ZIRLO alloy, (2) carbon ions implanted with 1×10^{16} ions/cm^2; (3) carbon ions implanted with 5×10^{16} ions/cm^2;(4) carbon ions implanted with 1×10^{17} ions/cm^2; (5) carbon ions implanted with 1×10^{18} ions/cm^2.

the binding energy of O1s is 530.2 eV, which suggests the oxygen at the surface exists as ZrO_2 as for implanted ZIRLO alloy. There are two peaks 530.2 and 531.4 eV as for as-received ZIRLO alloy, the 530.2 eV correspondents to the O1s binding energy of ZrO_2, while the 531.3 eV correspondents to the O1s binding energy of Nb_2O_5. With increasing the fluence, the relative

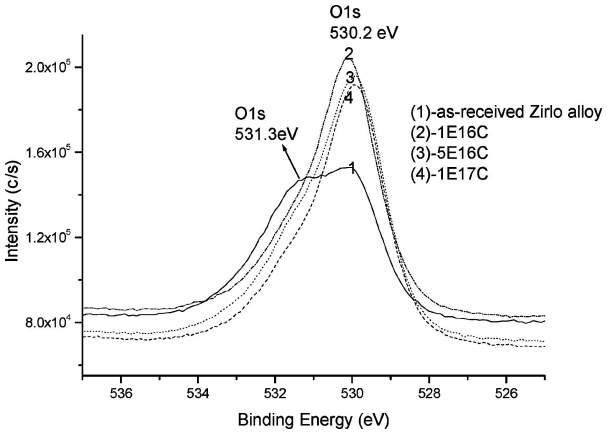

Figure 4 The XPS spectra of O1s peak in the implanted surface: (1) as-received ZIRLO alloy;(2)carbon ions implanted with 1×10^{16} ions/cm^2; (3) carbon ions implanted with 5×10^{16} ions/cm^2;(4)carbon ions implanted with 1×10^{17} ions/cm^2.

concentration of niobium in the surface layer declined because of carbon implantation, subsequently the peak of 531.3 eV declined quickly. Oxygen comes from residual gas in vacuum chamber, because the vacuum level of the target chamber of the MEVVA implanter is not very high. From the AES, we can determine that the fluence of carbon is higher, and the penetration depth of oxygen is greater.

3.2. The depth profile of the elements in the implanted surface layer

AES measurements to determine the concentration of elements in the surface layer as a function of depth were carried out using a PHI-610/SAM spectrometer. For the AES measurements, the sputter rate was approx. 30 nm/min. Curves (1)–(4) in Fig. 5 show AES spectra of ZIRLO alloy implanted with carbon ions using fluences of 0, 1×10^{16}, 5×10^{16}, 1×10^{17} ions/cm^2. The results show that the depths of oxygen in the oxide films are 18, 108,170, and 660 nm, respectively. The peak concentrations of carbon are approx. 9, 14 and 17%, corresponding to fluences of 1×10^{16}, 5×10^{16}, 1×10^{17} ions/cm^2, respectively. The depth corresponding to the peak concentration of carbon with 1×10^{16}, 5×10^{16}, 1×10^{17} ions/cm^2 fluences are approx. 144, 180, 190 nm, respectively. A computer simulation program, TRIM-96, was used to calculate the expected distribution of carbon (Fig. 6). From Fig. 6, the peak position of carbon is 78 nm. The peak positions of experiments are bigger than that of calculated value, 78 nm. These phenomena can be attributed to the thermal diffusion of carbon. Because the implantation was not employed at liquid nitrogen temperature, but at room temperature, the temperature of implanted samples was mainly depended on the beam current densities. From the Table I, it can be known that the temperature is about 100°C as for 1×10^{16} ions/cm^2 fluence, carbon diffuse a little. When the fluence is greater than 1×10^{16} ions/cm^2, the beam current densities are much bigger that of 1×10^{16} ions/cm^2 fluence, the temperature of them are over 200°C, therefore the carbon diffuse severely. From AES measurements, the carbon implantation enhanced the oxidization of ZIRLO alloy samples, the larger the fluence, the thicker is the zirconia oxide film of implanted samples.

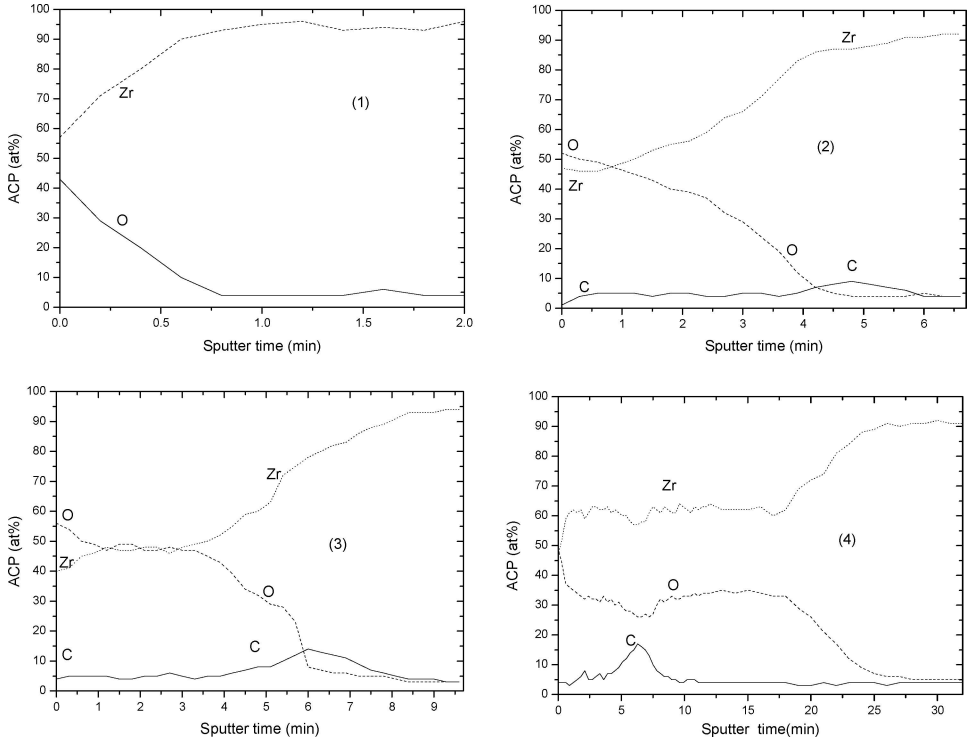

Figure 5 AES spectra of ZIRLO alloy implanted with carbon at (1) as-received ZIRLO alloy; (2) 1×10^{16} ions/cm^2; (3) 5×10^{16} ions/cm^2; (4) 1×10^{17} ions/cm^2.

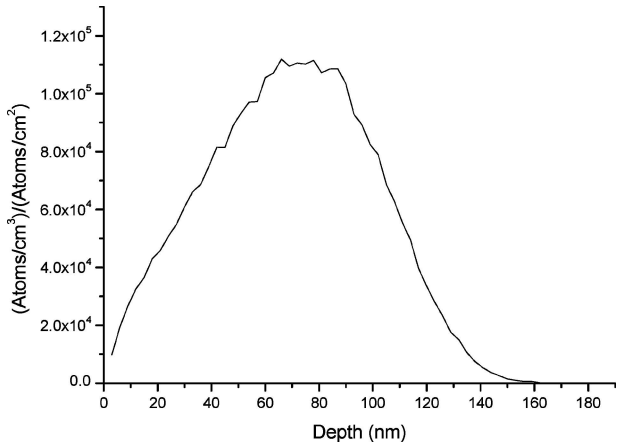

Figure 6 Distribution range of carbon ions determined by TRIM-96.

3.3. The phase structure in the implanted surface layer

The Glancing angle X-ray diffraction (GAXRD) was employed to investigate the phase structure characters in the implanted surface layer due to the carbon addition. From the AES of samples, the depth extent for the three fluences carbon–implanted ZIRLO alloy was about a few hundreds of nanometers. If conventional XRD is used, then the information is dominated by the matrix, while the information contributed by the thin film will be very little. The Glancing angle X-ray diffraction (GAXRD) with 0.3° glancing angle was employed in our experiment to study the phase characters of the carbon implantation ZIRLO alloy. The 0.3° diffraction angle corresponded to a theoretical penetration depth of about 55nm in the scale. So the 0.3°-angle was determined for the incident angle.

Fig. 7 shows the GAXRD spectra at 0.3° incident angle of implanted samples. From the observation of Fig. 7, it is clear that the as-received ZIRLO alloy is mainly composed of hexagonal alpha zirconium. As for implanted samples, there appeared hexagonal zirconia (H1-$ZrO_{0.35}$) and (H2-ZrO_2). The H1-$ZrO_{0.35}$ is compact, whose crystalline density is 36.4 atoms/nm^3; while the H2-ZrO_2 is loose, whose crystalline density is 9.6 atoms/nm^3. When the fluence is 1×10^{16} ions/cm^2, the intensity of compact H1-$ZrO_{0.35}$ is the largest in all the samples, the concentration of H1-$ZrO_{0.35}$ is the biggest. While the intensity of loose H2-ZrO_2 is the least in all the samples, the concentration of H2-ZrO_2 is the smallest. Subsequently, the oxide film of ZIRLO alloy implanted with 1×10^{16} ions/cm^2 is the most compact in all the samples. With increasing the implantation fluence, the intensity of compact H1-$ZrO_{0.35}$ declined, while the intensity of loose H2-ZrO_2 raised, subsequently the oxide films became looser and looser.

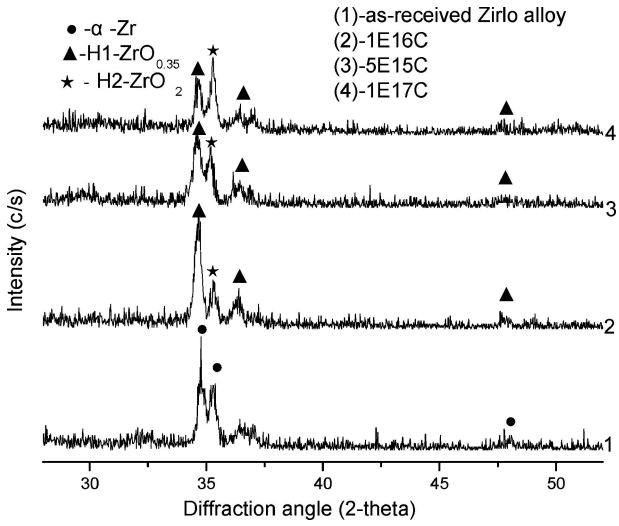

Figure 7 The GAXRD spectra at 0.3^0 incident angle of (1) as-received ZIRLO alloy; and implanted with C at (2) 1×10^{16} ions/cm^2; (3) 5×10^{16} ions/cm^2; and (4) 1×10^{17} ions/cm^2. α-Zr represents hexagonal alpha metallic zirconium, H1 represents hexagonal zircona (H-$ZrO_{0.35}$), whose crystalline cell density is 36.4 atoms/nm^3. H2 represents another hexagonal zirconia (H2-ZrO_2), whose crystalline cell density is 9.6 atoms/nm^3.

3.4. The microstructure of carbon implanted ZIRLO alloy in the surface layer

The microstructures of carbon implanted samples were examined by TEM. Although the grain size of the sputtered film may be different to that of the 1 mm sheet, the structure that would be seen in a 1 mm sheet is well represented by TEM studies of a sprayed film if the implanted fluence is high enough [7]. The thickness of all the sprayed ZIRLO alloy films was 50 nm. Part 1a and b in Fig. 8 show the polycrystalline structure obtained for the unimplanted ZIRLO alloy, the diameter of polycrystalline particles is about 13 nm. Part 2a–4a in Fig. 8 are bright field images of implanted samples, Part 2b–4b in Fig. 8 are selected area diffraction (SAD) pattern. Part 2a and b in Fig. 8 show the partially amorphous and crystal structures when the fluence is 1×10^{16} ions/cm^2. Most of the polycrystalline particles are spherical with 17 nm diameter. in this case, the implantation temperature is low, only 100°C, most of the defects during the implantation will be reserved, subsequently the structure changed from polycrystalline to partially amorphous, which consisted with others' report [7, 12]. When the fluence is 5×10^{16} ions/cm^2, the implanted surface layer changed into polycrystalline structure. Most of the polycrystalline particles are spherical and square with diameters ranging from 20 to 35 nm. This is probably attributed to the high temperature during the implantation. The implantation temperature in this fluence is high, up to 220°C, therefore, the polycrystalline particles grow much. When the fluence reached 1×10^{17} ions/cm^2, the implanted surface layer is still polycrystalline structure with 30 nm average diameter

TABLE II The relationship between the passive current density and carbon ion fluences

Fluence (ions/cm^2)	dpa	Passive current density (A/cm^2)
As-received ZIRLO alloy	0	1.7×10^{-5}
1×10^{16}	2.07	7.14×10^{-7}
5×10^{16}	10.3	1.06×10^{-6}
1×10^{17}	20.7	$1.5 \times 1\,0^{-6}$

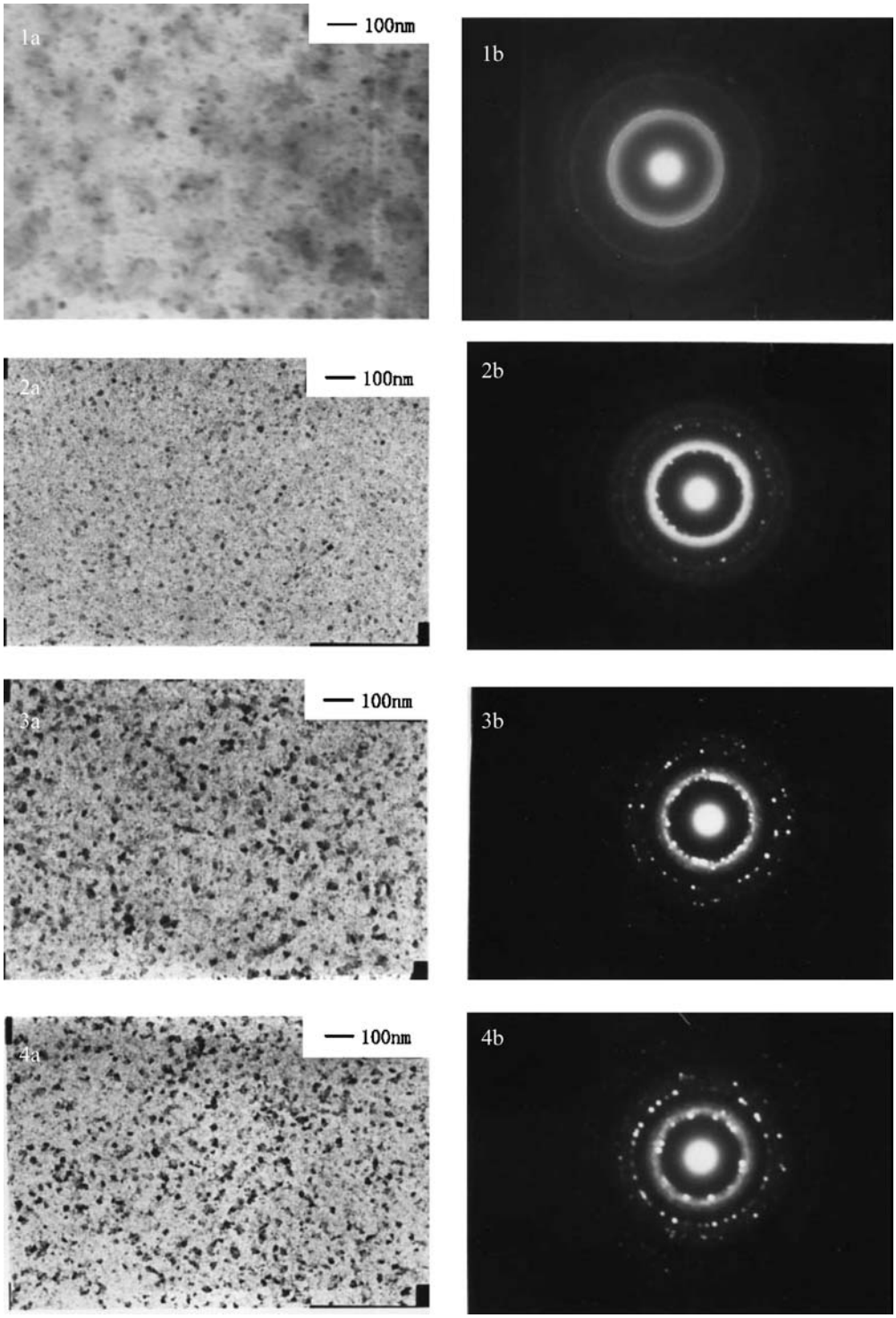

Figure 8 TEM of carbon implanted ZIRLO alloy at fluence range from 0 to 1×10^{17} ions/cm^2 (a) bright field image; (b) TEM selected area electron diffraction patterns (SAD): (1) as-received ZIRLO alloy, (2)1×10^{16} ions/cm^2, (3) 5×10^{16} ions/cm^2, (4) 1×10^{17} ions/cm^2.

in the implanted surface layer. This is also attributed to the high temperature during the implantation. In this fluence, the implantation temperature reached to 250°C, which leaded to the growth of polycrystalline particles.

3.5. The electrochemical behavior of the carbon-implanted ZIRLO alloy

Compared with each other, the potentiodynamic polarization curves of the as-received ZIRLO alloy and the ZIRLO alloy implanted with carbon-ions to a fluence ranging from $1 \times 10^{16}$to 1×10^{17} ions/cm^2 are summarized in Fig. 9. Fig. 10 plots the passive current density i_p as a function of fluence (values are summarized in Table II). From Figs 9 and 10, it was found that a significant improvement of corrosion resistance was achieved as for the implanted ZIRLO alloy. The higher the fluence, the large is the passive current density; subsequently the worse is the corrosion resistance of implanted samples. Fig. 11 plots the zero current potential as a function fluence (values are summarized in Table III), which shows that all the zero current potentials of implanted

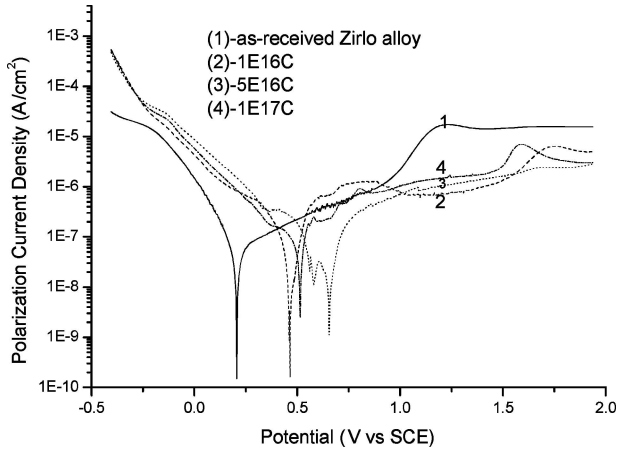

Figure 9 The potentiodynamic polarization curves in 1M H_2SO_4 solution of the as-received ZIRLO alloy and ZIRLO alloy implanted with carbon ions at a fluence of:(1) as-received ZIRLO alloy, (2) 1×10^{16} ions/cm^2, (3) 5×10^{16} ions/cm^2, (4) 1×10^{17} ions/cm^2.

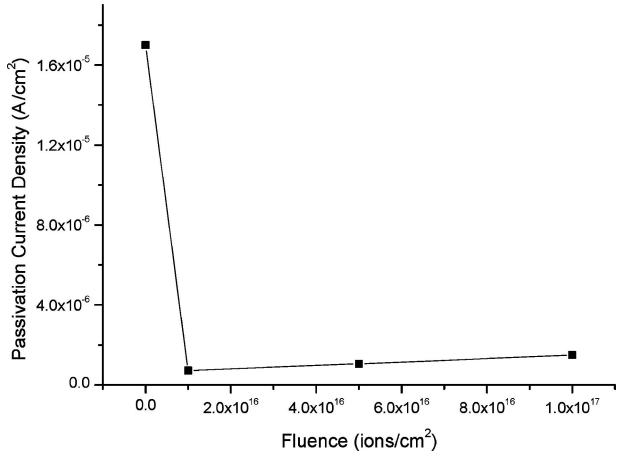

Figure 10 The dependence of the passivation current density, i_p, on the implanted fluences.

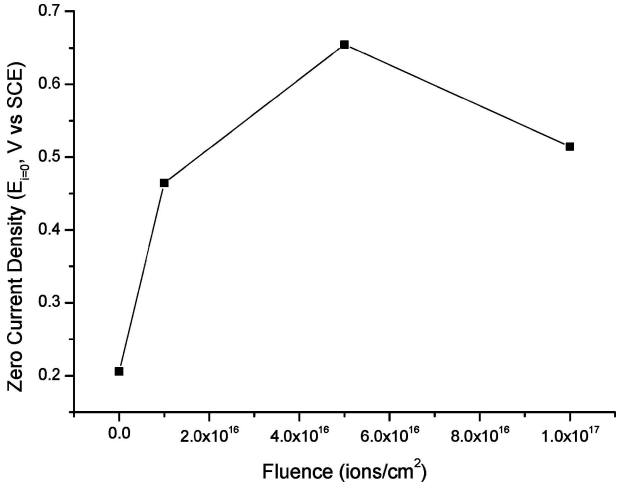

Figure 11 The dependence of the zero current potential ($E_{i=0}$) on the implanted fluences.

samples are more positive than that of as-received ZIRLO alloy, and subsequently the better is the corrosion resistance of the implanted samples. The results reflect by passive current densities are consistent with those reflect by zero current potentials as for samples.

3.6. The mechanism of the aqueous corrosion behavior by carbon ion implantation

It is well known that the formation of the passive film on surface of the ZIRLO alloy is an oxidation process. According to Pourbaix [13], there is an oxidation reaction that can take place at the ZIRLO alloy anode:

$$Zr(m) = Zr^{4+}(aq) + 4e^- \quad (1)$$

The cathodic reactions may be:

$$2H^+ + 2e^- = H_2(g) \quad (2)$$

As analyzed above, as for the unimplanted sample, it is mainly alpha zirconium, there is little oxidation protection in the surface of the sample, and anodic reaction of zirconium is easy to occur, subsequently the corrosion resistance of ZIRLO alloy is bad. From the results of XPS and AES, it is fact that the carbon implantation promoted the oxidation of ZIRLO alloy. The zirconia film acted as a barrier to reduce the anodic reaction, subsequently, the corrosion resistance of all the implanted samples is better than that of as-received ZIRLO alloy. The more compact is the oxide film, the more difficult is the anodic reaction of ZIRLO alloy, and the better is the corrosion resistance of implanted sample. It is known that the oxide film with 1×10^{16} fluence is the most compact in all the samples, subsequently the corrosion resistance is the best. From the TEM, the unimplanted sample is polycrystalline structure, while the sample with 1×10^{16} fluence is changed into partially amorphous, it is probably another main reason of raising the corrosion resistance. This result is consistent with other's [7, 12]. With increasing the fluence, the oxide film became looser and looser, subsequently the corrosion behavior is worse and worse.

On the other hand, when the target metal was implanted with ions, the surface layer was damaged. Different irritation ions lead to different damage efficiency. The depth dependence of damage level in the units of displacement per atom (dpa) was calculated by TRIM-96 computer program. The damage events were calculated and shown in Fig. 12. In the outermost layer,

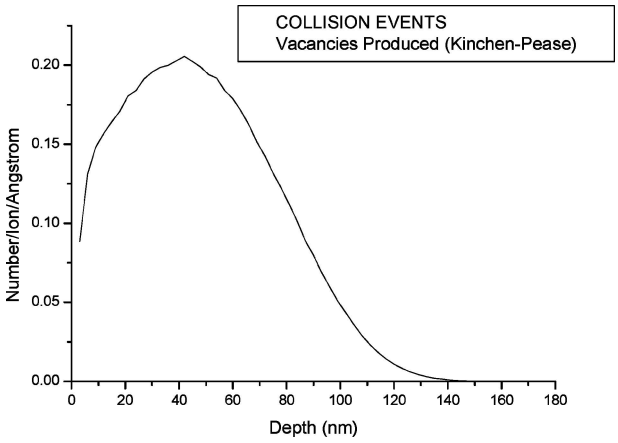

Figure 12 The depth dependence of damage level of carbon ions implantation.

TABLE III The relationship between zero current potential and the fluences

Fluence (ions/cm^2)	Zero current potential ($E_{i=0}$, V vs. SCE)
As-received ZIRLO alloy	0.206
1×10^{16}	0.4645
5×10^{16}	0.6545
1×10^{17}	0.5145

the damage efficiency of tin ion implantation is 0.0885 number/ion/angstrom. The damage level (represented by dpa) will be changed by the implanted fluence, shown in Table II. From Table II, it can be known the tendency that the carbon implantation enhanced the corrosion except for as-received ZIRLO alloy. With the damage level increasing, the passive current densities enhance. Up to now, many implantation corrosion mechanisms were proposed, such as the mechanism of enhancement of conductivity of oxide film by the change of energy band under implantation [14], electric conduction of the precipitates in the oxide films [15], the enhancement of oxide film cracks under implantation [16]. The basic effect of implantation is to create a lot of disorder of lattice atoms in oxide film, which changes the shape of the energy band and add some local conductive states inside the forbidden band along the collision tracts in the oxide films. The greater the fluence increases, the more serve the disorder forms, the more conductivity of the oxide film are and finally the easier the electrochemical corrosion. Therefore the implantation enhanced the corrosion.

4. Conclusions

The carbon was implanted into the ZIRLO alloy sample, from XPS and AES, it was found that the carbon ion implantation promoted the oxidation in the surface layer. From GAXRD, the unimplanted sample is mainly hexagonal alpha zirconium; there appeared H1-$ZrO_{0.35}$ and H2-ZrO_2 as for carbon implanted samples. The zircinia oxide film with 1×10^{16} ions/cm^2 is the most compact in all the samples, and the oxide film became looser and looser with increasing the fluence. From the TEM, it is fact that microstructure change from polycrystalline to partially amorphous structure, when the fluence is 5×10^{16} ions/cm^2, the microstructure changes to polycrystalline again, and the polycrystalline particles grow bigger. A significant improvement of corrosion resistance was achieved as for carbon implanted ZIRLO alloy. This is attributed to the oxidation protection. While the large the fluence, the worse is the corrosion resistance of implanted ZIRLO alloy sample. The reason is that the oxide film become looser and looser with increasing the fluence. The micro-structure of 1×10^{16} ions/cm^2 is changed into partially amorphous, which is probably another main reason of raising the corrosion resistance. The damage level (represented by dpa) increases linearly with increasing the fluence, subsequently the corrosion behavior of implanted samples declines with the fluence.

Acknowledgement

Special thanks should be given to the Ministry of Science and Technology of China for research funding (MSTC No. G 2000067207-1). Authors would like to thank Analysis Center of Tsinghua University for partial financial support.

References

1. Y. ETOH, S. SHIMADA and K. KIKUCHI, *J. Nucl. Sci. Tech.* **29**(12) (1992) 1173.
2. JIAN XU, XINDE BAI and YUDIAN FAN, *J. Mater. Sci.* **35** (2000) 6225.
3. S. J. LEE, H. S. KWON, W. KIM and B. H. CHOI, *Mater. Sci. Engng. A* **263** (1991) 23.
4. JIAN XU, XINDE BAI, AN JIN and YUDIAN FAN, *J. Mater. Sci. Lett.* **19** (2000) 1633.
5. V. ASHWORTH, D. BAXTER, W. A. GRANT, R. P. M. PROCTER and T. C. WELLINGTON, *Corros. Sci.* **16** (1976) 775.
6. G. K. HUBLE and E. MCCAFFERTY, *ibid.* **20** (1980) 103.
7. X. D. BAI, D. H. ZHU and B. X. LIU, *Nucl. Instr. Meth. Phys. Res. B* **103** (1995) 440.
8. N. J. MIKKLELSEN and C. A. STRAEDE, *Surf. Coat. Techn.* **51** (1992) 152.
9. J. I. ONATE, F.ALONSO and A. GARCIA, *Thin Solid Films* **317** (1998) 471.
10. YONGLIANG LI, TONGHE ZHANG and XIAOYAN WANG, *Surf. Coat. Tech.* **128/129** (2000) 205.
11. C. D. WAGNER, W. M. RIGGS, L. E. DAVIS, J. F. MOULDER and G.E. MUILENBERG (eds.), "A Reference Book of Standard Data for Use in X-ray Photoelectron Spectroscopy" (Perkin-Elmer Corporation, Physical Electronics Division, 6509 Flying Cloud Drive, Eden Prairie, Minnesota 55344) p. 100.
12. M. F. STROOSNIJDER, J. D. SUNDERKOTTER, M. J. CRISTOBAL, H. JENETT, K. ISENBUGEL and M. A. BAKER, *Surf. Coat. Techn.* **83** (1996) 205.
13. M. POURBAIX, "Atlas of Electrochemical Equilibria in Aqueous Solutions" (N.A.C.E., Houstan, TX, 1974) p. 223.
14. U. Stimming, *Electrochemica Acta* **31**(4) (1986) 415.
15. P. J. SHIRVINGTON, *J. Nucl. Mater.* **37** (1970) 177.
16. R. A. PLOT, *ibid.* **91** (1980) 332.

Received 23 August
and accepted 29 November 2004